

# JGR Space Physics

## RESEARCH ARTICLE

10.1029/2020JA027846

### Key Points:

- The spatial distribution of nitric oxide (NO) in the high-latitude Southern Hemisphere middle atmosphere varies during geomagnetic storms
- Initial NO increases coincide with geomagnetic latitudes where 30–300 keV precipitating electron fluxes are high
- Transport of NO away from source regions by strong ( $\sim 20\text{--}30\text{ m s}^{-1}$ ) eastward winds in the Antarctic upper mesosphere is observed over 1–3 days

### Correspondence to:

D. A. Newnham,  
dawn@bas.ac.uk

### Citation:

Newnham, D. A., Rodger, C. J., Marsh, D. R., Hervig, M. E., & Clilverd, M. A. (2020). Spatial distributions of nitric oxide in the Antarctic wintertime middle atmosphere during geomagnetic storms. *Journal of Geophysical Research: Space Physics*, 125, e2020JA027846. <https://doi.org/10.1029/2020JA027846>

Received 6 FEB 2020

Accepted 14 MAY 2020

Accepted article online 14 JUN 2020

## Spatial Distributions of Nitric Oxide in the Antarctic Wintertime Middle Atmosphere During Geomagnetic Storms

D. A. Newnham<sup>1</sup> , C. J. Rodger<sup>2</sup> , D. R. Marsh<sup>3,4</sup> , M. E. Hervig<sup>5</sup> , and M. A. Clilverd<sup>1</sup> 

<sup>1</sup>British Antarctic Survey, Cambridge, UK, <sup>2</sup>Department of Physics, University of Otago, Dunedin, New Zealand,

<sup>3</sup>Atmospheric Chemistry Division, National Center for Atmospheric Research, Boulder, CO, USA, <sup>4</sup>Priestley International Centre for Climate, University of Leeds, Leeds, UK, <sup>5</sup>GATS, Driggs, ID, USA

**Abstract** Energetic electron precipitation leads to increased nitric oxide (NO) production in the mesosphere and lower thermosphere. NO distributions in the wintertime, high-latitude Southern Hemisphere atmosphere during geomagnetic storms are investigated. NO partial columns in the upper mesosphere at altitudes 70–90 km and in the lower thermosphere at 90–110 km have been derived from observations made by the Solar Occultation For Ice Experiment (SOFIE) on board the Aeronomy of Ice in the Mesosphere (AIM) satellite. The SOFIE NO measurements during 17 geomagnetic storms in 2008–2014 have been binned into selected geomagnetic latitude and geographic latitude/longitude ranges. The regions above Antarctica showing the largest instantaneous NO increases coincide with high fluxes of 30–300 keV precipitating electrons from measurements by the second-generation Space Environment Monitor (SEM-2) Medium Energy Proton and Electron Detector (MEPED) instrument on the Polar-orbiting Operational Environmental Satellites (POES). Significant NO increases over the Antarctic Peninsula are likely due to precipitation of  $>30\text{ keV}$  electrons from the radiation belt slot region. NO transport is estimated using Horizontal Wind Model (HWM14) calculations. In the upper mesosphere strong eastward winds (daily mean zonal wind speed  $\sim 20\text{--}30\text{ m s}^{-1}$  at 80 km) during winter transport NO-enriched air away from source regions 1–3 days following the storms. Mesospheric winds also introduce NO-poor air into the source regions, quenching initial NO increases. Higher up, in the lower thermosphere, weaker eastward winds ( $\sim 5\text{--}10\text{ m s}^{-1}$  at 100 km) are less effective at redistributing NO zonally.

## 1. Introduction

### 1.1. Background Information

Energetic particle precipitation (EPP) in the middle and upper polar atmosphere increases abundances of odd nitrogen ( $\text{NO}_x = \text{N} + \text{NO} + \text{NO}_2$ ) and odd hydrogen ( $\text{HO}_x = \text{H} + \text{OH} + \text{HO}_2$ ) (Baker et al., 2018; Brasseur & Solomon, 2005; Mironova et al., 2015; Sinnhuber et al., 2012). In the upper mesosphere and lower thermosphere, at altitudes between  $\sim 65$  and 140 km, ionization by precipitating energetic electrons and protons driven by space weather events produces  $\text{NO}_x$  primarily as nitric oxide (NO).  $\text{NO}_x$  and  $\text{HO}_x$  species react catalytically with ozone ( $\text{O}_3$ ) present in the stratosphere and mesosphere (Jackman & McPeters, 2004). Ozone changes resulting from enhanced levels of  $\text{NO}_x$  and  $\text{HO}_x$  can affect the radiative balance, temperature, and large-scale dynamics of the atmosphere. EPP during solar proton events (SPEs) and by electrons thereby provides a mechanism linking space weather, via changes in the chemical composition in the middle atmosphere, to natural climate variability (e.g., Arsenovic et al., 2016; Baumgaertner et al., 2011; Semeniuk et al., 2011; Seppälä et al., 2009, 2013).

The spectrum of electrons precipitating into the atmosphere at high latitudes covers a wide span of energies, from keV to MeV (Baker et al., 2018; Turunen et al., 2009). Auroral NO is produced in abundance in the lower thermosphere at 100–120 km by low-energy (1–30 keV) electrons (Marsh et al., 2004). During geomagnetic storms, radiation belt electrons with relativistic energy ( $\sim 1\text{--}4\text{ MeV}$ ) cause ionization down to  $\sim 50\text{ km}$  (Horne et al., 2005, 2009). Frequently occurring magnetospheric substorms may also produce large cumulative changes in polar mesospheric  $\text{O}_3$  and  $\text{HO}_x$  (Seppälä et al., 2015). Medium-energy electron (MEE) precipitation with energies in the range  $\sim 30\text{--}1,000\text{ keV}$  creates ionization at altitudes  $\sim 60\text{--}90\text{ km}$ .

## 1.2. Previous Studies

Satellite observations and ground-based passive millimeter-wave measurements show that MEE precipitation produces direct impacts on mesospheric chemistry (e.g., Andersson et al., 2018; Arsenovic et al., 2019; Newnham et al., 2018, and references therein; Zawedde et al., 2019). In the Southern Hemisphere (SH), the strongest OH enhancements during MEE precipitation are at altitudes 70–78 km and in the longitude sector 150°W to 30°E, i.e., in the region poleward of the South Atlantic Magnetic Anomaly (SAMA) region (Andersson et al., 2014).

The Solar Occultation For Ice Experiment (SOFIE) instrument (Gordley et al., 2009) on board the Aeronomy of Ice in the Mesosphere (AIM) satellite has operated since 14 May 2007. Analysis of the multiyear SOFIE NO data sets (Hendrickx et al., 2015, 2017, 2018), combined with model calculations (Smith-Johnsen et al., 2017), suggests that geomagnetic activity is the dominant source of short-term NO variability throughout the high-latitude lower thermosphere, whereas mesospheric NO variability is mainly due to the indirect effect of downward-transported NO originating from ~75 km. Lee et al. (2018) used Michelson Interferometer for Passive Atmospheric Sounding (MIPAS) data to identify direct NO<sub>x</sub> production by MEE down to ~55 km. A semiempirical model based on MIPAS data sets (Funke et al., 2017) allows computation of EPP-modulated reactive nitrogen (NO<sub>y</sub>) species and wintertime downward fluxes through the stratosphere and mesosphere. An empirical model (Bender et al., 2019) for NO in the mesosphere (~60–90 km) has been derived using data from another satellite instrument, the SCanning Imaging Absorption spectroMeter for Atmospheric CHartography (SCIAMACHY), complementing and extending the Nitric Oxide Empirical Model (NOEM; Marsh et al., 2004) and Sub-Millimeter Radiometer (SMR) Acquired Nitric Oxide Model Atmosphere (SANOMA; Kiviranta et al., 2018).

Simulations of the atmospheric effects of EPP using the specified dynamics version of the Whole Atmosphere Community Climate Model (WACCM 4) (Marsh et al., 2013) were improved by including MEE ionization (Pettit et al., 2019). WACCM-D (Verronen et al., 2016) and WACCM-SIC (Kovács et al., 2016) allow more detailed representations of *D* region chemistry to be performed in WACCM simulations. WACCM-D simulations (Smith-Johnsen et al., 2018), while underestimating NO at 90–110 km, showed that including MEE ionization is important for modeling NO production and transport at altitudes of 80 km and below. However, determining realistic estimates of the precipitating MEE fluxes from satellite-based energetic particle measurements remains a major challenge (Rodger et al., 2010).

## 1.3. This Work

In this study we investigate the geographic and geomagnetic latitude ( $\Lambda$ ) distributions of wintertime NO in the high-latitude SH middle atmosphere during selected geomagnetic storms within a 7-year period, 2008–2014. The aim of the work is to better understand the variation of NO in the middle atmosphere, including direct production by auroral electrons and MEE, and horizontal transport processes that potentially redistribute NO<sub>x</sub> species away from their source regions. Our results identify areas that need to be better understood for atmospheric model development and requirements for further acquisition and analysis of observational data.

The manuscript layout is as follows. Section 2 describes data sets used in the study, outlines geomagnetic conditions during 2008–2014, and characterizes the selected geomagnetic storms. The methodology for processing and analyzing the satellite observations using geographic and geomagnetic latitude binning and superposed epoch analysis (SEA) and the empirical wind model configuration are described. The results of the analyses of the NO partial columns, Polar-orbiting Operational Environmental Satellites (POES) electron flux observations, and wind model data poleward of 60°S are presented in section 3. The NO distributions are discussed in section 4 in terms of competing localized NO production and transport mechanisms. The main conclusions are summarized and potential areas for future research are outlined in section 5.

## 2. Data Sets

### 2.1. Geomagnetic Indices

Auroral electrojet (*AE*) index (Davis & Sugiura, 1966) and disturbance storm time (*Dst*) index (Yokoyama & Kamide, 1997) data were used to assess geomagnetic conditions during 2008–2014. *AE* has been shown

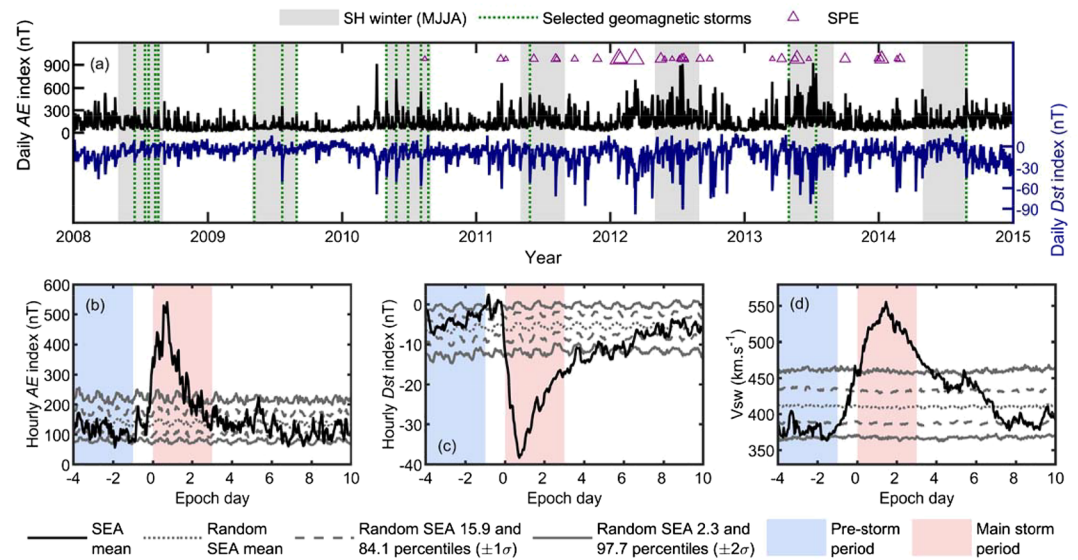


**Figure 1.** (a) Daily AE index and daily Dst index for 2008–2014. The shaded gray areas indicate the SH winter months (May–August). The green dotted vertical lines show the occurrences (epoch day 0) of the 17 selected geomagnetic storms. Purple triangles show SPEs, where the triangle size indicates maximum proton flux on a logarithmic scale. Note that the AE and Dst indices are plotted on different scales. SEA of hourly (b) AE index, (c) Dst index, and (d) solar wind speed ( $V_{sw}$ ) for the selected geomagnetic storms. The shaded blue areas indicate a 3 day prestorm period (epoch days  $-4$  to  $-2$ ) and the shaded red areas a 3 day main storm period (epoch days 0 to 2). The dotted gray curves are the mean values of the random SEA of each data set, and the dashed and solid gray curves show the 15.9 and 84.1 percentiles ( $\pm 1\sigma$ ) and 2.3 and 97.7 percentiles ( $\pm 2\sigma$ ), respectively, of the random distributions.

(Hendrickx et al., 2015) to be more strongly related to EPP-produced NO than the planetary Ap index, which is derived from midlatitude observations (Dieminger et al., 1996).

The daily AE index and Dst index data sets (both available from [wdc.kugi.kyoto-u.ac.jp/dstdir](http://wdc.kugi.kyoto-u.ac.jp/dstdir)) are plotted in Figure 1a. Increased geomagnetic activity corresponds to higher AE index and minima in Dst. SPE occurrences are shown by triangles, with the triangle size indicating maximum proton flux on a logarithmic scale. The largest SPEs produced comparatively modest maximum 10 MeV proton fluxes of  $6,310 \text{ protons cm}^{-2} \text{ sr}^{-1} \text{ s}^{-1}$  on 24 January 2012 and  $6,530 \text{ protons cm}^{-2} \text{ sr}^{-1} \text{ s}^{-1}$  on 8 March 2012 (for a full list of SPEs affecting the Earth environment, see <ftp://ftp.swpc.noaa.gov/pub/indices/SPE.txt>).

Our analysis focuses on SH wintertime (May, June, July, and August [MJJA]) when NO is long-lived at latitudes  $>60^\circ\text{S}$  (geographic). The 17 periods of increased geomagnetic activity during 2008–2014 identified by Hendrickx et al. (2018), when the AE index increases by more than two standard deviations of the data set, are used. The dates of the 17 events are 15 June, 13 July, 23 July, 10 August, and 18 August 2008; 7 May, 22 July, and 30 August 2009; 2 May, 29 May, 30 June, 4 August, and 24 August 2010; 28 May 2011; 1 May and 14 July 2013; and 27 August 2014. These geomagnetic storm occurrences, marked by green dashed vertical lines in Figure 1, are relatively isolated from neighboring storms and do not overlap in time with SPEs. More powerful geomagnetic storms with lower Dst indices occurred during the 2011–2013 winters, but these events are closely spaced and overlap SPEs and so are not included in our analysis.

SEA of hourly AE and Dst indices and solar wind speed ( $V_{sw}$ , available from <http://umtof.umd.edu/pm/crn/>) was performed using epochs defined by the 17 selected geomagnetic storms. The solar wind data are from the Charge, Element, Isotope Analysis System (CELIAS)/Mass Time-of-Flight spectrometer–Proton Monitor (MTOF-PM) on the Solar and Heliospheric Observatory (SoHO) spacecraft (Ipavich et al., 1998). Random SEAs were performed with ensembles of 1,000 sets of 17 epochs randomly selected from the entire 2008–2014 wintertime (MJJA) AE and Dst indices, and  $V_{sw}$ , data sets. The mean, 15.9 and 84.1 percentiles ( $\pm 1\sigma$ ), and 2.3 and 97.7 percentiles ( $\pm 2\sigma$ ) of the random SEA distributions were calculated. The SEA results for the three data sets are shown in Figures 1b–1d. The shaded blue areas in the plots highlight the 3 days before the storms, from the start of epoch day  $-4$  to the end of epoch day  $-2$ ,



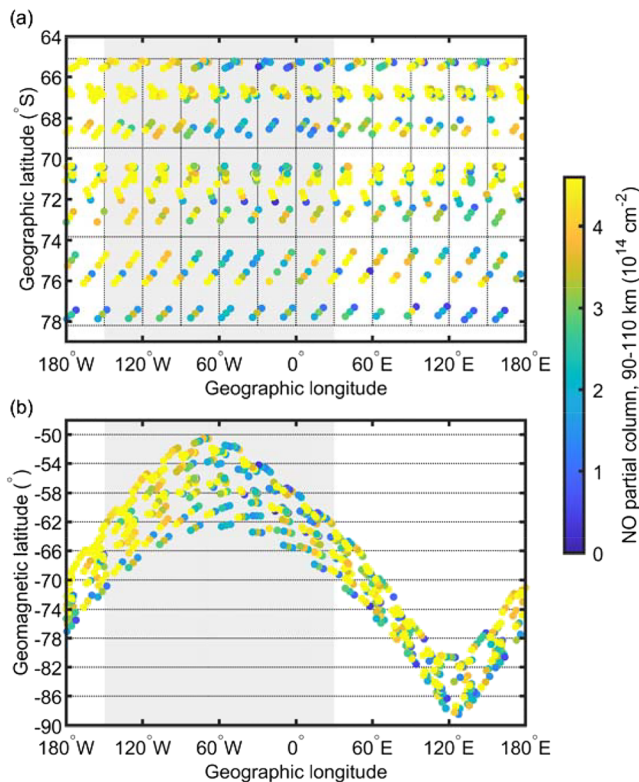


**Figure 2.** (a) Geographic and (b) geomagnetic binning ranges for SOFIE NO data. The horizontal and vertical dotted lines show the limits of the selected latitudinal and, in (a) only, geographic longitudinal ranges, respectively. The locations of the filled circles are the geographic and geomagnetic coordinates of observed SOFIE NO partial columns at 90–110 km during the main storm period (epoch days 0 to 2) of the 17 selected geomagnetic storms. The colored circles represent the values of the NO partial columns. The gray shaded panels indicate the range of longitudes (150°W to 30°E) of the SAMA, located equatorward of the plotted data.

when *AE*, *Dst*, and *V<sub>sw</sub>* are at background levels. The superposed *AE* and *Dst* show maximum deviations during epoch day 0, whereas *V<sub>sw</sub>* changes more slowly and reaches a maximum the following day. The minimum superposed hourly *Dst* of  $-39 \text{ nT}$  indicates moderate geomagnetic activity occurs, on average, at the peak of the selected storms (Yokoyama & Kamide, 1997). The shaded red areas in the plots mark a 3 day main storm period (from the start of epoch day 0 to the end of epoch day 2) when *AE* index is above the 84.1 percentile ( $>1\sigma$ ) of the random SEA distribution. While *AE* index recovers to the background level ( $<1\sigma$ ) by the end of epoch day 2, *Dst* index and *V<sub>sw</sub>* remain perturbed until at least epoch day 6, indicating ongoing magnetospheric processes that could drive further energetic electron precipitation (EEP) into the atmosphere after the main storm phase.

## 2.2. AIM-SOFIE

In this work we used NO number density vertical profiles from the SOFIE version 1.3 data set (Hervig et al., 2019), which have been filtered to remove polar mesospheric cloud contamination and smoothed by boxcar averaging, resulting in a nominal 3 km vertical resolution (mission data file SOFIE\_L2m\_2007135\_2017026\_NO\_den\_filt\_sm\_01.3.nc, available on the SOFIE web page <http://sofie.gats-inc.com/sofie/index.php>, last access: 8 October 2019). The SOFIE measurements in the SH used here correspond to spacecraft sunset measurements, which have smaller overall errors than have sunrise measurements, which were made in the Northern Hemisphere (NH) during 2007–2017.

NO partial columns were calculated from the SH SOFIE number density profiles over the altitude ranges 70–90 km (upper mesosphere) and 90–110 km (lower thermosphere). The NO partial column lower range of 70–90 km covers altitudes where changes in NO abundance due to MEE are likely to be greatest although, as noted earlier (section 1.1), MEE ionization can occur down to  $\sim 60 \text{ km}$ . The SOFIE NO uncertainty analysis of Hervig et al. (2019) was used to estimate the NO partial column uncertainties. The geographic coordinates of the NO observations were converted to corrected geomagnetic coordinates using GEO2CGM code (Matthes

et al., 2017), which uses the International Geomagnetic Reference Field (IGRF-12) internal field model (Thébault et al., 2015) for magnetic field calculations. The individual NO partial columns were then binned and averaged into the geographic longitude/latitude ranges and geomagnetic latitude ranges defined in Figure 2. For geographic binning, NO observations were combined to determine best estimates and accuracy (Palmer, 2014) for the partial columns in each of 36 bins covering  $30^\circ$  longitude intervals (i.e.,  $0^\circ$  to  $30^\circ\text{E}$ ,  $30^\circ\text{E}$  to  $60^\circ\text{E}$ , etc.) and three equally spaced latitude ranges:  $65.10^\circ\text{S}$  to  $69.47^\circ\text{S}$  (mean latitude  $67.3^\circ\text{S}$ ),  $69.47^\circ\text{S}$  to  $73.83^\circ\text{S}$  (mean latitude  $71.7^\circ\text{S}$ ), and  $73.83^\circ\text{S}$  to  $78.20^\circ\text{S}$  (mean latitude  $76.0^\circ\text{S}$ ). For calculating best estimates of the geomagnetic zonal mean partial columns, ten  $4^\circ$  wide bins covering  $\Lambda = -50^\circ$  to  $-90^\circ$  were used. The daily data in each bin of the 3 day prestorm periods (geomagnetic storm epoch days  $-4$  to  $-2$ ) and the main storm periods (epoch days 0 to 2) of the 17 geomagnetic storms were then averaged. SEA was also carried out to determine the daily mean partial columns for the six individual epoch days  $-1$  to 4 in each of the bins. Random SEA were performed with ensembles of 1,000 sets of 17 epochs randomly selected from the entire 2008–2014 wintertime (MJJA) SOFIE NO data set. The mean, 15.9 and 84.1 percentiles ( $\pm 1\sigma$ ), and 2.3 and 97.7 percentiles ( $\pm 2\sigma$ ) of the random SEA distributions were calculated.

## 2.3. POES-MEPED

In this study we used daily median electron precipitation fluxes from the Medium Energy Proton and Electron Detector (MEPED) (Evans & Greer, 2004; Hendry et al., 2017; Rodger et al., 2010; Whittaker et al., 2014) provided by the National Oceanic and Atmospheric Administration (NOAA) and European Organisation for the Exploitation of Meteorological Satellites (EUMETSAT) POES. The data were proton



corrected and zonally averaged as described in Newnham et al. (2018). Fluxes were binned into the following seven invariant magnetic latitude (Kivelson & Russell, 1995) and  $L$ -shell (McIlwain, 1961) ranges:  $-54^\circ$  to  $-58^\circ$  ( $L \sim 2.89$ – $3.56$ ),  $-58^\circ$  to  $-62^\circ$  ( $L \sim 3.56$ – $4.54$ ),  $-62^\circ$  to  $-66^\circ$  ( $L \sim 4.52$ – $6.04$ ),  $-66^\circ$  to  $-70^\circ$  ( $L \sim 6.04$ – $8.55$ ),  $-70^\circ$  to  $-74^\circ$  ( $L \sim 8.55$ – $13.16$ ),  $-74^\circ$  to  $-78^\circ$  ( $L \sim 13.16$ – $23.13$ ), and  $-78^\circ$  to  $-82^\circ$  ( $L \sim 23.13$ – $51.63$ ). The extent of reliable POES data ( $\Lambda = -54^\circ$  to  $-82^\circ$ ;  $L \sim 2.89$ – $51.63$ ) overlaps the SOFIE observations and includes the regions of auroral and radiation belt electron deposition. For geographic binning, daily median EEP flux was calculated in  $5^\circ$  latitude bins (i.e.,  $90^\circ\text{S}$  to  $85^\circ\text{S}$ ,  $85^\circ\text{S}$  to  $80^\circ\text{S}$ , etc.) and  $30^\circ$  longitude bins ( $0$ – $30^\circ$ ,  $30$ – $60^\circ$ , etc.). Geographic locations were calculated by tracing magnetic field from the satellite location down to 100 km altitude using IGRF-12. POES data within the SAMA and Weddell Sea regions, where EEP fluxes have previously proved unreliable (Rodger et al., 2013), were discarded. Therefore, the binned NH POES data which are unaffected by the SAMA are also presented. The likely distributions of precipitating electron fluxes for the data gaps in the SH geographic region poleward of  $60^\circ\text{S}$  were estimated using fluxes for the bins containing NH geomagnetic conjugate points corresponding to selected locations in the SAMA-affected SH region.

The electron precipitation fluxes in the 100–300 keV range (produced by subtracting the POES MEPED electron fluxes for the  $>300$  keV channel from those of the  $>100$  keV channel) will ionize constituents in the neutral atmosphere at  $\sim 70$ – $90$  km altitude (Turunen et al., 2009). Electron precipitation within the 30–100 keV range will produce peak ionization at  $\sim 78$ – $102$  km. EEP ionization and NO production at  $\sim 100$ – $110$  km is dominated by auroral electrons ( $\sim 10$  keV), which typically enter the atmosphere at  $\Lambda \sim 65$ – $75^\circ$  during low geomagnetic activity (Barth et al., 2003; Barth & Bailey, 2004).

#### 2.4. Horizontal Wind Model

The Horizontal Wind Model 2014 (HWM14, version HWM14.123114, last access: 3 July 2019) (Drob et al., 2015) was used to estimate horizontal wind speeds and directions. The HWM14 calculations were undertaken for 80 and 100 km altitudes, for each day from 00:00 hr to 23:00 hr UT at 1 hr intervals, and on a geographic grid of latitudes  $60^\circ\text{S}$  to  $85^\circ\text{S}$  at  $5^\circ$  intervals and  $30^\circ$  longitude intervals. The hourly wind data show large diurnal variability due to the specification of planetary waves and the migrating diurnal, semidiurnal, and terdiurnal tides in HWM14. While atmospheric wave and tide processes temporarily displace air masses, NO transport on longer time scales of one or more days will be dominated by the daily mean winds. The hourly data within epoch days 0 to 2 of each of the selected geomagnetic storms were therefore averaged to remove short-term, diurnal variability and provide empirical estimates of the daily mean meridional and zonal winds in the upper mesosphere and lower thermosphere.

### 3. Results

In this section the SOFIE NO data analysis, together with POES electron flux measurements, magnetic local time (MLT), and HWM14 calculations are presented. In section 4 we interpret the observed NO changes in the upper mesosphere and lower thermosphere in response to geomagnetic storms. Longitude ranges in the SH are given for a clockwise direction on polar plots; for example,  $180^\circ$  to  $120^\circ\text{W}$  means a  $60^\circ$  segment between  $180^\circ$  (E/W) and  $120^\circ\text{W}$ .

#### 3.1. Geomagnetic Zonal Mean Distributions of NO

We use the NO partial columns binned into selected geomagnetic latitude ranges to establish the geomagnetic zonal mean distributions of NO and identify where the largest storm time increases occur. Geomagnetic zonal mean NO partial columns at 70–90 and 90–120 km are shown in Figure 3 for the 3 day prestorm background (i.e., from the start of epoch day  $-4$  to the end of epoch day  $-2$ ), the 3 day main storm period (i.e., from the start of epoch day 0 to the end of epoch day 2), and the storm time changes in partial column. The storm time changes in NO partial column are the differences between the main storm and prestorm partial columns. The corresponding mean partial columns and the 15.9 and 84.1 percentiles ( $\pm 1\sigma$ ) and 2.3 and 97.7 percentiles ( $\pm 2\sigma$ ) of the randomly sampled SOFIE data set are shown by the superimposed gray lines. NO partial columns above the  $1\sigma$  and  $2\sigma$  levels of the random distributions indicate changes in NO abundance associated with increased geomagnetic storm activity rather than background variability that occurs in the absence of geomagnetic storms. The prestorm NO partial columns at 70–90 km (Figure 3a) and at 90–110 km (Figure 3d) are below the random mean values. Lower NO abundance is expected

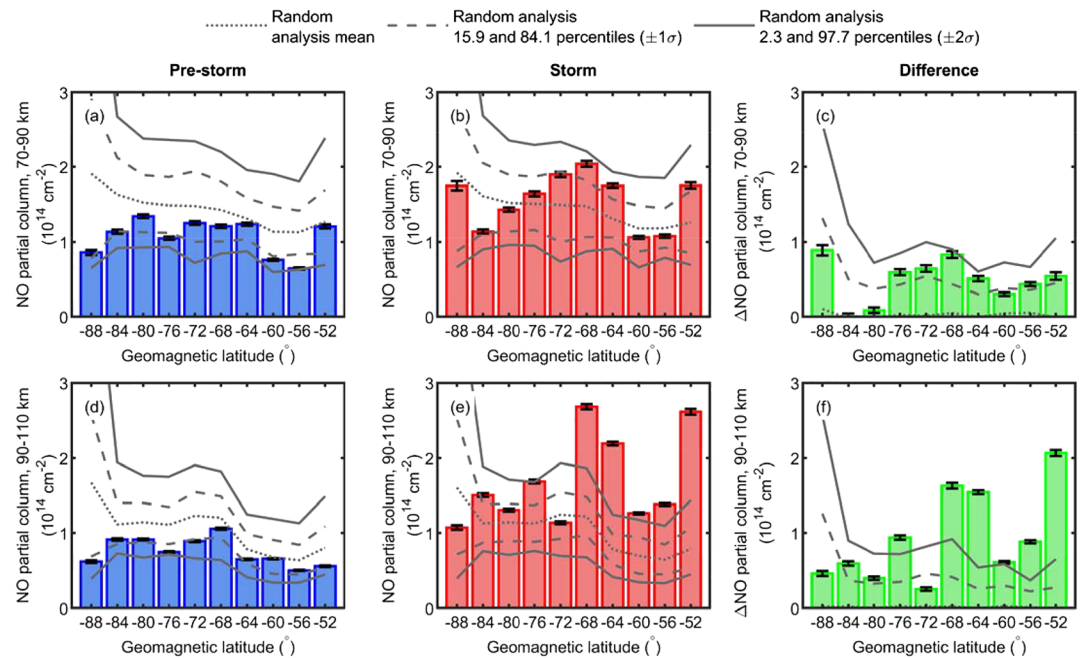


**Figure 3.** Geomagnetic zonally averaged NO partial columns at 70–90 km for (a) the prestorm period (epoch days –4 to –2), (b) the main storm period (epoch days 0 to 2), and (c) the storm time change in NO partial column. (d–f) The corresponding results for NO partial column at 90–110 km. The errors bars show the estimated measurement uncertainties for the SOFIE NO partial columns.

during the prestorm periods when geomagnetic activity is low when contrasted with randomly selected time periods. Furthermore, the selected geomagnetic storms are sufficiently well separated that the prestorm periods should not overlap NO enhancements arising from previous storms. In the intervals between the end of each storm and the next prestorm period, NO produced by EPP during the storm will be redistributed away from the main source regions and diluted by incoming NO-poor air transported from outside the source regions. NO is also lost by photolysis in the sunlit mesosphere and lower thermosphere (Shimazaki, 1984) and, below 65 km, by conversion to  $\text{NO}_2$  and other  $\text{NO}_x$  species (Solomon et al., 1982). In contrast, the “prestorm” periods of the randomly selected epochs potentially overlap geomagnetic storms when NO production increases. During the storm period, the NO partial columns for both altitude ranges (i.e., 70–90 and 90–110 km) increase in each geomagnetic latitude bin except  $\Lambda = -84^\circ$  at 70–90 km. However, at 70–90 km the NO increases reach or exceed the  $1\sigma$  level only for the  $\Lambda = -52^\circ$  and  $\Lambda = -64^\circ$  to  $-72^\circ$  bins. The largest NO increase  $(0.829(46) \times 10^{14} \text{ cm}^{-2})$  at 70–90 km that reaches the  $2\sigma$  significance level is in the  $\Lambda = -68^\circ$  bin. Larger NO increases occur at 90–110 km, with the  $\Lambda = -52^\circ$  to  $-68^\circ$  and  $\Lambda = -76^\circ$  bins exceeding the  $2\sigma$  level. At these higher altitudes the NO increases are above the  $1\sigma$  level in all latitude bins except  $\Lambda = -72^\circ$  and  $\Lambda = -88^\circ$ . The largest increases at 90–110 km are at  $\Lambda = -52^\circ$   $(2.065(41) \times 10^{14} \text{ cm}^{-2})$ , followed by  $\Lambda = -68^\circ$   $(1.544(26) \times 10^{14} \text{ cm}^{-2})$  and  $\Lambda = -64^\circ$   $(1.631(38) \times 10^{14} \text{ cm}^{-2})$ .

### 3.2. Geographic Distributions of NO and Lag Times

In this section the NO partial columns, binned by geographic latitude/longitude, are used to identify regions where the largest storm time increases in NO occur. Analysis of the time evolution of the NO geographic distributions provides further evidence of the main NO production regions and horizontal transport of NO. Maps of the geographic latitude/longitude binned NO partial columns at 70–90 and 90–110 km for the pre storm background (epoch days –4 to –2), the main storm period (epoch days 0 to 2), and the storm time changes in partial column are shown in Figure 4. For the upper mesosphere (altitudes 70–90 km), the largest and most significant NO increases of up to  $2.46(12) \times 10^{14} \text{ cm}^{-2}$  occur over a relatively small region, covering longitudes  $180^\circ$  to  $120^\circ\text{W}$  in the  $67.3^\circ\text{S}$  latitude bin, with smaller poleward increases. These regions are within the  $\Lambda = -60^\circ$  to  $-70^\circ$  oval and overlap the geomagnetic zonal means with the largest NO

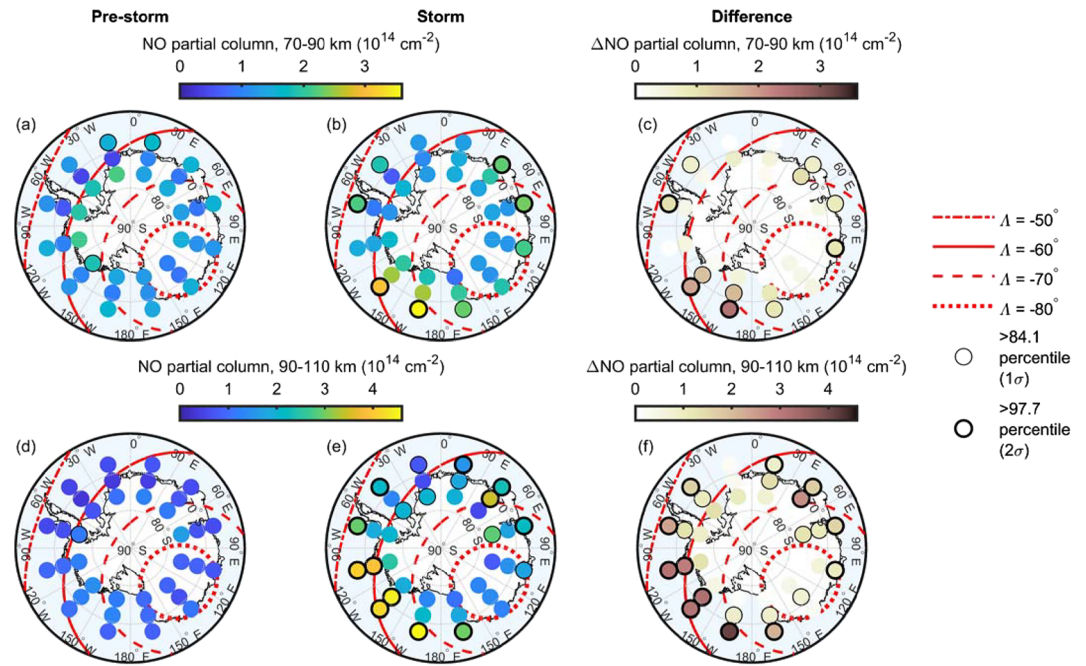


**Figure 4.** Maps of the SH and Antarctica poleward of 60°S with the filled color circles showing the observed NO partial columns at 70–90 km for (a) the prestorm period (epoch days –4 to –2), (b) the main storm period (epoch days 0 to 2), and (c) the storm time change in NO partial column. (d–f) The corresponding results for NO partial column at 90–110 km. Thick black outer circles indicate data above the 97.7 percentile (>2σ) of the random SEA distribution. Thinner black outer circles indicate data between the 84.1 and 97.7 percentiles (>1σ and <2σ), and data without black outer circles are below the 84.1 percentile (<1σ) of the random SEA distribution. The dash-dotted, solid, dashed, and dotted red lines show the geomagnetic latitudes  $\Lambda = -50^\circ$ ,  $-60^\circ$ ,  $-70^\circ$ , and  $-80^\circ$ , respectively, calculated for 1 January 2012 and an altitude of 80 km using GEO2CGM code (Matthes et al., 2017). Note the different color scales for partial column values in the top and bottom plots.

increases (Figure 3c). Within the rest of the  $-60^\circ$  to  $-70^\circ$  region poleward of 60°S, at 30–60°E in the 67.3°S and 71.7°S bins, there are smaller but significant (>1σ) NO increases of  $\sim 0.85(9) \times 10^{14} \text{ cm}^{-2}$ . However, at 120°W to 30°E including the Antarctic region poleward of the Weddell Sea, increases are small and of low significance (<1σ). In contrast, significant (>2σ) increases of up to  $1.023(69) \times 10^{14} \text{ cm}^{-2}$  occur in the two diametrically opposite 67.3°S bins at 90–120°E and at 90–60°W (west of the Antarctic Peninsula), both well outside of  $\Lambda = -60^\circ$  to  $-70^\circ$ . These NO enhancements, at  $\Lambda = -52^\circ$  and  $-80^\circ$ , could arise from direct NO production in these regions or from NO transported over 1–2 days from source regions at intermediate geomagnetic latitudes where 30–300 keV electron flux increases are more typically expected. The likely contributions to the observed NO distributions from these two mechanisms will be discussed in the next section. Smaller NO increases at 70–90 km are found for the remaining geographic bins encompassing the 60°S to 80°S range of the SOFIE SH data.

In the lower thermosphere (i.e., altitudes 90–110 km), NO increases during the main storm period are larger than those at 70–90 km and extend across a wider area. The largest (up to  $4.10(9) \times 10^{14} \text{ cm}^{-2}$ ) and most significant increases at 90–110 km are in the 180° to 90°W quadrant in the 67.3°S and 71.7°S bins, with smaller increases at 30–60°E. The enhanced regions include part of the  $\Lambda = -60^\circ$  to  $-70^\circ$  region, but significant NO increases also occur outside this range, over  $\Lambda = -50^\circ$  to  $-60^\circ$  and  $\Lambda = -70^\circ$  to  $-78^\circ$ . NO increases at 90–110 km are smaller for the remaining geographic bins encompassing the  $\sim 60$ –80°S range of the SOFIE SH observations.

Figures 5 and 6 show the changes in NO partial column with longitude and epoch day in each of the three geographic latitude ranges, at altitude ranges 70–90 and 90–110 km, respectively. On epoch day –1 the  $\Delta\text{NO}$  values are close to 0, except for a peak at 150–120°W and 67.3°S in the 70–90 km partial column. This initial NO increase may be due to localized MEE precipitation arising from increased geomagnetic activity in the latter part of this day. As geomagnetic activity increases on epoch day 0,



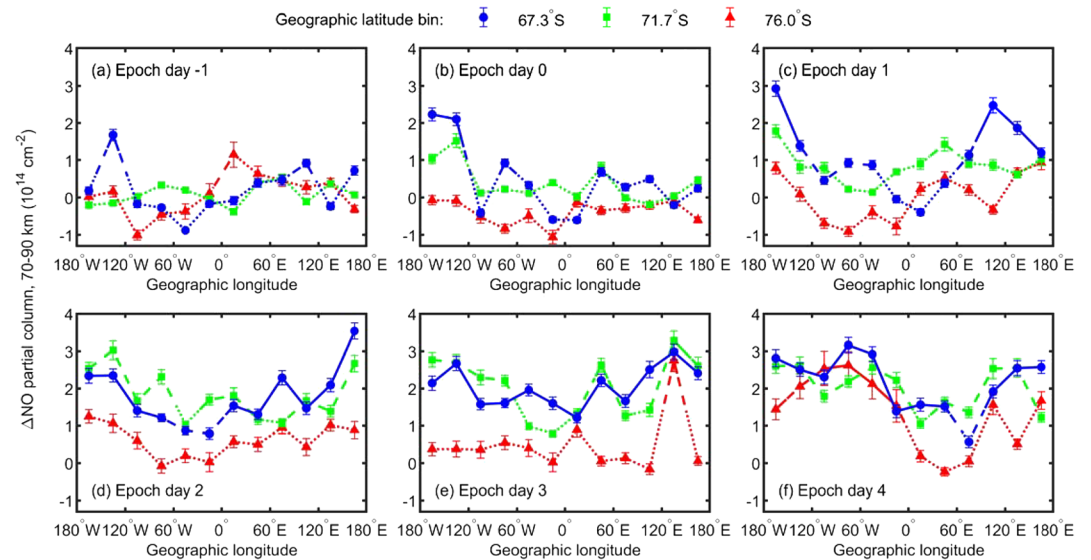


**Figure 5.** Change in NO partial column at 70–90 km with longitude from prestorm values, for geomagnetic storm epoch days –1 to 4 at three geographic latitude ranges: 65.10°S to 69.47°S (filled blue circles and dashed blue lines labeled “67.3°S”), 69.47°S to 73.83°S (filled green squares and dotted green lines labeled “71.7°S”), and 73.83°S to 78.20°S (filled red triangles and solid red lines labeled “76.0°S”). Solid lines indicate data above the 97.7 percentile ( $>2\sigma$ ) of the random SEA distribution. Dashed lines indicate data between the 84.1 and 97.7 percentiles ( $>1\sigma$  and  $<2\sigma$ ), and dotted lines show data below the 84.1 percentile ( $<1\sigma$ ) of the random SEA distribution. The error bars are the uncertainties on the best estimates of the NO partial columns, calculated using published SOFIE measurement errors (Hervig et al., 2019).

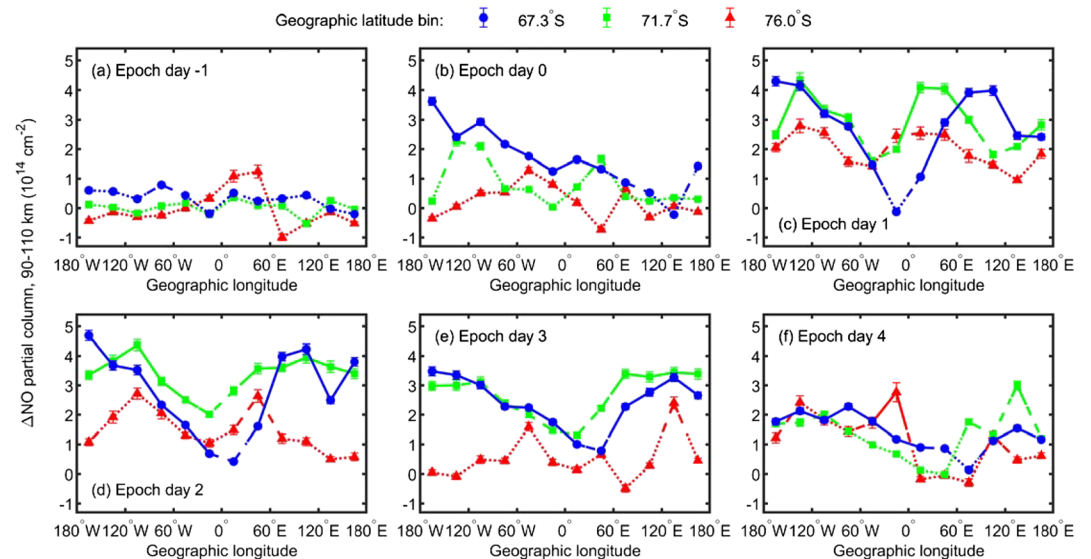


**Figure 6.** Change in NO partial column at 90–110 km with longitude from prestorm values, for geomagnetic storm epoch days –1 to 4 at three geographic latitude ranges: 65.10°S to 69.47°S (filled blue circles and dashed blue lines, labeled “67.3°S”), 69.47°S to 73.83°S (filled green squares and dotted green lines, labeled “71.7°S”), and 73.83°S to 78.20°S (filled red triangles and solid red lines, labeled “76.0°S”). Solid lines indicate data above the 97.7 percentile ( $>2\sigma$ ) of the random SEA distribution. Dashed lines indicate data between the 84.1 and 97.7 percentiles ( $>1\sigma$  and  $<2\sigma$ ), and dotted lines show data below the 84.1 percentile ( $<1\sigma$ ) of the random SEA distribution. The errors bars are the uncertainties on the best estimates of the NO partial columns, calculated using published SOFIE measurement errors (Hervig et al., 2019).

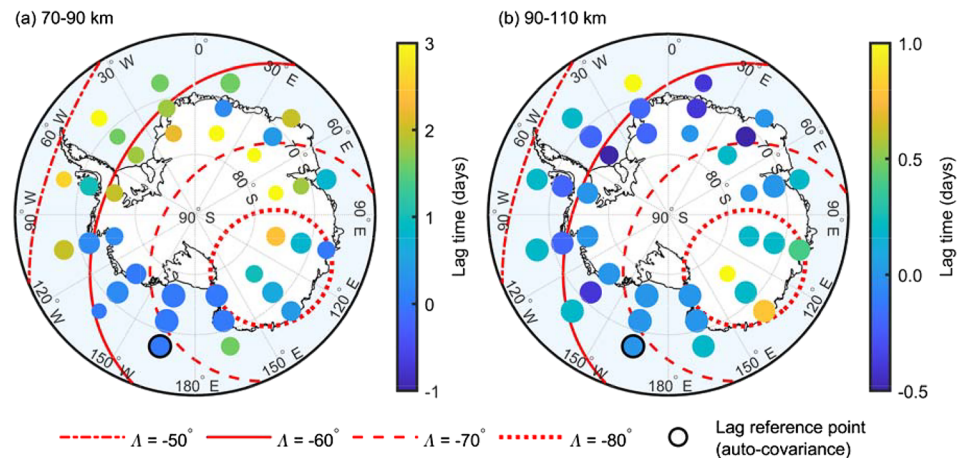


**Figure 7.** Maps of the SH and Antarctica poleward of 60°S with the filled color circles showing the lag times of NO partial columns at (a) 70–90 km and (b) 90–110 km corresponding to the highest cross-covariance against the indicated lag reference point. The circle size indicates the maximum cross-covariance at that location, where the lag reference point has a normalized cross-covariance (autocovariance) value of 1 and 0 lag time. The dash-dotted, solid, dashed, and dotted red lines are as described in Figure 4. Note that the lag time ranges (color scales) differ for (a) and (b).

the region of significant ( $>2\sigma$ )  $\Delta$ NO at 70–90 km extends over 180° to 120°W with smaller increases at 90–60°W. The most significant initial NO increases at 90–110 km cover a wider range of longitudes, 180°W to 0° at 67.3°S. In both altitude ranges the  $\Delta$ NO values are generally lower over 0° to 150°E for all three latitude ranges. On epoch day 1 the longitudinal pattern of  $\Delta$ NO changes with two main peaks in each latitude range. The highest and most significant  $\Delta$ NO values are in the 67.3°S data at 180–120°W and 90–150°E at 70–90 km, with smaller increases at 71.7°S and 76.0°S. The largest NO increases during the six epoch days occur on epoch day 2, 1 day after the highest geomagnetic activity as indicated by the maximum in  $AE$  index and minimum  $Dst$  index. The maximum  $\Delta$ NO is between 150°E to 180° at 70–90 km and at 180° to 150°W at 90–110 km, both in the 67.3°S bins. Afterward, on epoch days 3 and 4, the longitudinal peaks become less distinct and the NO increases spread over a wider longitude range. On epoch days 1–3, the NO partial columns at 90–110 km show an almost sinusoidal variation at 67.3°S and 71.7°S, with minima close to longitude 0°. Lower NO abundance in the 0° longitude region, corresponding to  $\Lambda \sim -60^\circ$ , suggests EEP flux and NO production decreases here  $\sim 24$  hr after the start of the geomagnetic storms. Localized variabilities in EEP flux will be discussed further in the POES MEPED results. In the highest-latitude bin, 76.0°S, the highest  $\Delta$ NO at both 70–90 and 90–110 km occurs 2–3 days after the highest geomagnetic activity with a distinct peak at 150°E to 180° on epoch day 3 and the highest levels over 150°W to 0° on epoch day 4. In the lower-latitude bins, 67.3°S and 71.7°S,  $\Delta$ NO at 70–90 km remains high on epoch days 3–4, whereas at 90–110 km  $\Delta$ NO decreases on consecutive days to reach levels similar to those at 76.0°S on epoch day 4.

Figure 7 shows the results of a cross-covariance analysis of the geographically binned NO partial columns. The lag times, indicated by the color scale of the plotted points on the maps, are with respect to the reference point data in the 67.3°S, 180° to 210° bin where the highest storm time increases in NO at 70–90 and 90–110 km are observed (Figure 4). The lag times correspond to the maximum cross-covariance in the time series of binned NO partial columns at each location. The maximum cross-covariance at each location is indicated in the plots by circle size, where the lag reference point has a normalized cross-covariance (autocovariance) value of 1. For the altitude range 70–90 km (Figure 7a) the lag times are  $\sim 0$ –1 days at 90°E to 90°W, which correspond to the locations where the highest NO increases occur, and also for some points within 0° to 60°E. These very short lag times suggest that direct production by MEE dominates the observed NO increases in these regions. At longitudes 90°W to 0° including the Weddell Sea area, lag times at 70–90 km are up to 2–3 days. These longer lag times indicate that the smaller NO increases in these regions are associated with MEE precipitation occurring after the main storm period (i.e., after epoch days 0 to 2) and transport from other locations. At 90–110 km

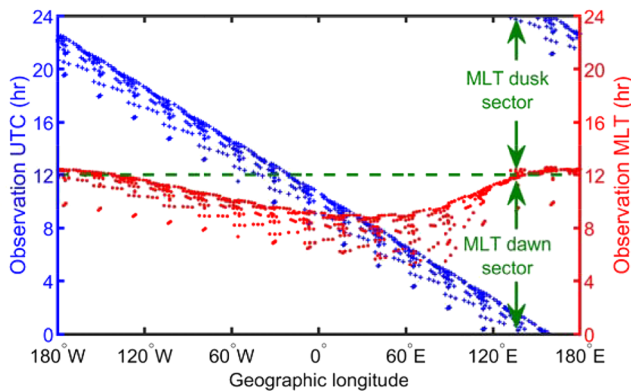


**Figure 8.** SOFIE NO observation times in coordinated universal time (UTC, shown as blue crosses) and magnetic local time (MLT, shown as filled red circles). The plotted points correspond to SH sunset SOFIE NO observations made on epoch days 0 to 2 of the geomagnetic storms selected for this study.

(Figure 7b) the NO lag times are generally smaller than those at 70–90 km. The highest lag times of up to a day are in the  $\Lambda > 70^\circ$  region where there is a high flux of auroral electrons and also eastward of the reference point at  $67.3^\circ\text{S}$ . In contrast, at higher geographic latitudes eastward of the reference point, lag times are negative indicating increases in NO occurring up to a day earlier than those at the reference point. These earlier NO increases at 90–110 km suggest earlier increases in precipitating electron flux in these regions ( $\Lambda \sim -58^\circ$  to  $-66^\circ$ ) compared to the reference point ( $\Lambda \sim -68^\circ$ ). This NO production mechanism will be discussed further in the context of observed POES MEPED 30–100 and 100–300 keV electron fluxes. The overall smaller lag times at 90–110 km suggest that observed NO increases in the lower thermosphere are dominated by direct EEP during the main storm phase and transport has less influence on observed NO distributions at these altitudes than those in the upper mesosphere.

### 3.3. MLT Variability of SOFIE Observations

In this section we investigate whether the MLT of SOFIE measurements make a significant contribution to the observed variations in NO abundance with location. Larger EEP fluxes are expected in the MLT dawn sector compared to the dusk sector (van de Kamp et al., 2018), producing higher ionization and NO production (Allison et al., 2017; Isono et al., 2014). Thus, it is important to assess whether the MLT differs significantly for SOFIE observations made at different locations, which would lead to variations in NO production and distribution.

The International Radiation Belt Environment Modeling library (<https://craterre.onera.fr/prbem/irbem/description.html>, last update: 22 May 2019) was used to convert the SOFIE observation times in coordinated universal time (UTC) to MLT. The UTC to MLT calculations were performed assuming a fixed altitude of 80 km, since tests showed that using altitudes from 70 to 110 km produced negligible changes to the determined MLT values. The variations of the observation times with longitude are shown in Figure 8. The AIM spacecraft, with SOFIE on board, is in Sun-synchronous orbit, and solar occultation at each longitude occurs at a similar UTC each day, with long-term drifts over the 2008–2014 time frame as the satellite orbit and instrument pointing changes. The calculations show that the SOFIE observations used in this study are predominantly in the MLT dawn sector, between 05:00 and 12:30 MLT. The SOFIE measurements used in this study are found to be within a fairly narrow MLT range inside or close to the dawn sector, and we conclude that differing measurement times are not a major cause of the observed differences in NO abundance with location.

### 3.4. POES MEPED Energetic Electron Distributions

In this section the POES MEPED observations in the SH and NH are used to identify the locations and temporal variations of enhanced energetic electron flux during the geomagnetic storms. Figure 9 shows maps of the geographical distributions of mean POES electron fluxes in the 30–100 and 100–300 keV energy ranges during the main storm period (epoch days 0 to 2), for the SH poleward of  $60^\circ\text{S}$  and for the NH poleward of  $50^\circ\text{N}$ . The NH plots extend further equatorward to cover the entire  $\Lambda = -60^\circ$  to  $-70^\circ$  region. In the SH (Figures 9a and 9c), POES data from  $90^\circ\text{W}$  to  $60^\circ\text{E}$  overlapping the SAMA are excluded due to proton contamination caused by proximity to the SAMA. For other SH longitudes, where electron fluxes are meaningful, the highest values in both energy ranges are within a section of the  $\Lambda = -60^\circ$  to  $-70^\circ$  region at  $150^\circ$ – $90^\circ\text{W}$ . Outside of this region the POES electron fluxes during the geomagnetic storms are typically lower by 50% or more.

At high northern latitudes the POES observations are not affected by the SAMA, and electron fluxes are meaningful at all longitudes. Furthermore, the POES fluxes close to geomagnetic conjugate points in the NH can be used to infer electron fluxes at the corresponding SH locations adversely affected by the SAMA. Five Antarctic locations (see Table 1 for details) within, or neighboring, the SH region affected by SAMA have been selected as reference points for comparison of the POES SH and NH conjugate data. The Antarctic sites are recognized locations with defined geographic coordinates, four of which correspond to Antarctic research stations. However, it should be noted that we do not use ground-based observations



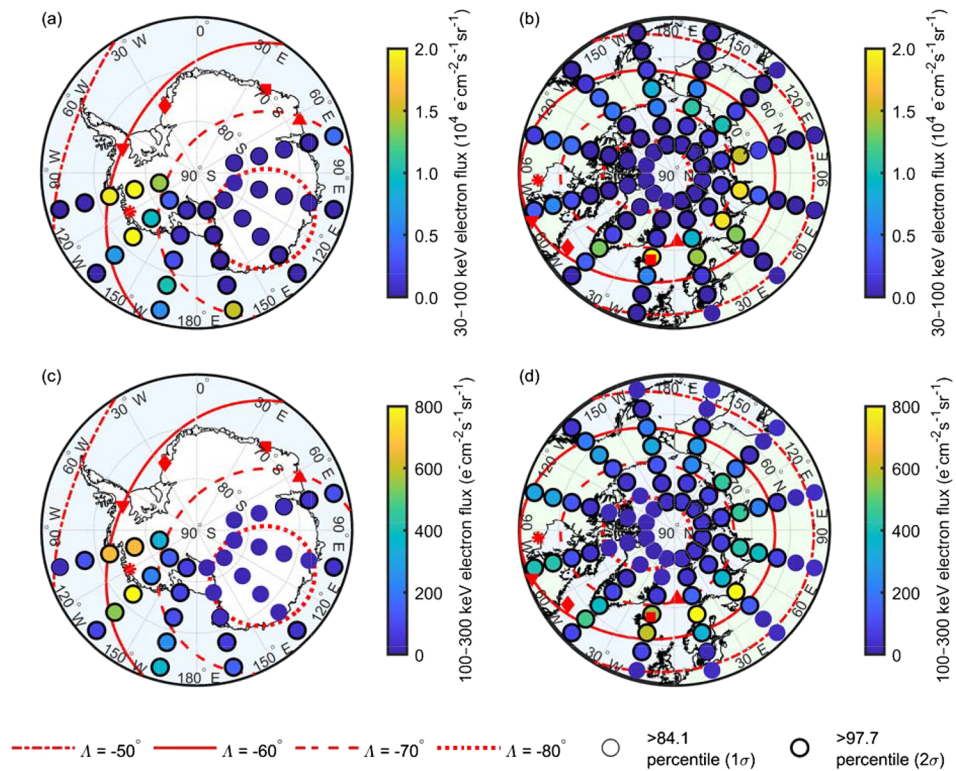


**Figure 9.** Maps of (a, c) the SH and Antarctica at 60–90°S and (b, d) the Northern Hemisphere at 50–90°N showing 30–100 and 100–300 keV electron fluxes for the main storm period (epoch days 0 to 2) estimated from POES MEPED measurements. Thick black outer circles indicate data above the 97.7 percentile ( $>2\sigma$ ) of the random SEA distribution. Thinner black outer circles indicate data between the 84.1 and 97.7 percentiles ( $>1\sigma$  and  $<2\sigma$ ), and data without black outer circles are below the 84.1 percentile ( $<1\sigma$ ) of the random SEA distribution. The dash-dotted, solid, dashed, and dotted red lines are as described in Figure 4. The red symbols show selected SH locations and their conjugate points in the NH. Note that the electron flux ranges (color scales) differ between the top plots (a and b) and the bottom plots (c and d).

data from these stations in this study. The NH conjugate locations at an altitude of 80 km above the five Antarctic locations have been calculated for year 2012 using the Virtual Ionosphere, Thermosphere, Mesosphere Observatory (VITMO) model (<https://omniweb.sci.gsfc.nasa.gov/vitmo/cgm.html>). Each of the SH locations and their corresponding NH conjugates are identified by different red symbols on the maps in Figure 9. Although 30–100 and 100–300 keV electron fluxes in the NH (Figures 9b and 9d) are more than an order of magnitude smaller than those in the SH, the regions of higher flux during the geomagnetic storms can be seen to extend over a larger section of the  $\Lambda = 60^\circ$  to  $70^\circ$  oval. Comparing the POES data close to the five indicated NH conjugates with the corresponding Antarctic locations suggests that electron fluxes within the SH oval increase clockwise from 150°W and are highest equatorward of 60°S, beyond the extent of the SH map. Higher fluxes of 30–300 keV electrons are expected to produce more NO directly at 70–110 km, whereas the NO partial columns observed by SOFIE do not show correspondingly large storm time enhancements in these regions. Possible reasons for these discrepancies between the geographic distributions of MEE flux and NO abundance will be discussed in the next section.

**Table 1**

*Geocentric Spherical (Geographic) Coordinates of Five Antarctic Locations, Corrected Geomagnetic (CGM) Coordinates, and Their NH Conjugate Locations*

Location (all Antarctica)	Geographic location	CGM latitude	CGM longitude	Conjugate location
Bakutis Coast, Marie Byrd Land	75.00°S, 120.00°W	−64.50°	−14.06°	54.70°N, 86.88°E
Sky-Blu Field Station, Eastern Ellsworth Land	74.85°S, 71.57°W	−60.00°	8.53°	51.16°N, 71.43°W
Halley VI Research Station, Brunt Ice Shelf, Caird Coast	75.57°S, 24.49°W	−62.26°	30.29°	56.35°N, 55.15°W
Syowa Station, East Ongul Island, Queen Maud Land	69.00°S, 39.58°E	−66.74°	72.93°	66.74°N, 15.23°W
Mawson Station, Mac Robertson Land	67.60°S, 62.87°E	−70.57°	91.54°	72.25°N, 2.21°E

*Note.* The sites have been selected as reference points for comparison of the POES SH and NH conjugate electron data.

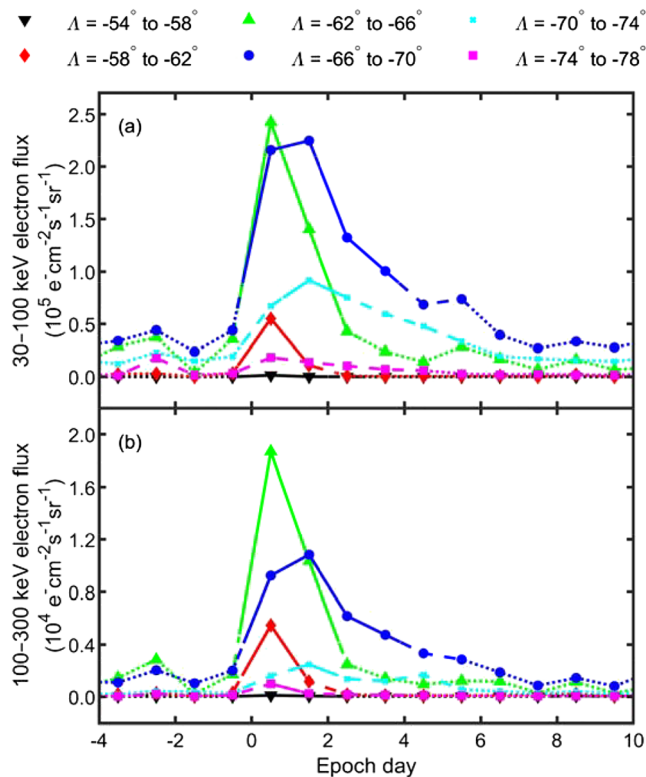


**Figure 10.** SEA results for daily mean 30–100 and 100–300 keV electron flux estimates at six geomagnetic latitude ranges. Solid lines indicate data above the 97.7 percentile ( $>2\sigma$ ) of the random SEA distribution. Dashed lines indicate data between the 84.1 and 97.7 percentiles ( $>1\sigma$  and  $<2\sigma$ ), and dotted lines show data below the 84.1 percentile ( $<1\sigma$ ) of the random SEA distribution.

Figure 10 shows the SEA for daily mean POES 30–100 and 100–300 keV electron flux observations in six geomagnetic latitude bands. The plots cover epoch days  $-4$  to  $10$  in order to show the initial prestorm background flux levels and differing temporal variations over the 10 days following the start of the geomagnetic storms. The highest fluxes in both energy ranges are at  $\Lambda = -62^\circ$  to  $-66^\circ$  during epoch day  $0$ , with the maximum 30–100 keV electron flux in this zone more than an order of magnitude higher than that at 100–300 keV. In this latitude range, and also for the smaller instantaneous flux increases at  $\Lambda = -58^\circ$  to  $-62^\circ$ , the increases are short-lived and fluxes return to prestorm levels by epoch day  $2$ . The second highest electron fluxes occur at  $\Lambda = -66^\circ$  to  $-70^\circ$ . For this latitude range, and at even higher latitudes ( $\Lambda = -70^\circ$  to  $-78^\circ$ ) where fluxes are lower, the fluxes peak on epoch day  $1$  and return slowly to background levels over several days. Fluxes in both energy ranges at  $\Lambda = -66^\circ$  to  $-70^\circ$  exceed prestorm levels and are above  $1\sigma$  of the random SEA distributions, until epoch day  $5$ . The variation of the POES fluxes suggests that while direct NO production above  $70$  km will be dominated by geomagnetic-storm-driven EEP at  $\Lambda = -60^\circ$  to  $-70^\circ$  coincident with deviations in the *AE* and *Dst* indices and higher solar wind speed, significant contributions to enhanced NO could continue for a further three or more days at higher geomagnetic latitudes ( $|\Lambda| > 65^\circ$ ). However, later NO production could be difficult to identify in observations as a separate direct NO source because, on similar time scales, long-lived NO is transported considerable horizontal distances and vertically downward from the thermosphere in the wintertime polar vortex.

### 3.5. NO Transport by Horizontal Winds

In this section the effect of transport on redistributing NO in the high-latitude SH region is considered, using calculated horizontal wind data. Zonal and meridional wind speeds and directions at altitudes of  $80$  and  $100$  km, calculated using HWM14, are superimposed on the maps

in Figure 11. The daily mean empirical model data for dates corresponding to epoch days  $0$  to  $2$  of the geomagnetic storms have been geographically binned with the same  $30^\circ$  longitude ranges as for the SOFIE NO and POES electron data analyses, but in  $5^\circ$  latitude bands from  $60^\circ\text{S}$  to  $90^\circ\text{S}$ . Model winds at both altitudes are predominantly eastward (clockwise in the plots). The winds are stronger at  $80$  km (Figure 11a) than at  $100$  km (Figure 11b), reaching  $20\text{--}30\text{ m s}^{-1}$  at  $60\text{--}70^\circ\text{S}$  and further poleward in the longitude range  $180^\circ$  to  $30^\circ\text{W}$ . These strong winds are expected to rapidly transport NO away from its source regions, primarily at  $\Lambda = -60^\circ$  to  $-70^\circ$  for MEE production and at higher geomagnetic latitudes for auroral NO. At  $100$  km the winds are generally lighter, with maximum speed of  $\sim 10\text{ m s}^{-1}$  at  $60\text{--}70^\circ\text{S}$  and within the  $|\Lambda| > 80^\circ$  region above East Antarctica, suggesting that at that altitude, NO produced by auroral electrons is transported more slowly. However, NO molecules descending from the lower thermosphere can undergo faster horizontal movement once entrained in mesospheric air masses.

## 4. Discussion

The NO spatial distributions in the SH wintertime middle atmosphere during geomagnetic storms provide insights into the complex, interacting processes including NO production by different EEP mechanisms, horizontal transport and mixing of air masses, and vertical downward movement of NO. In this section the potential roles of these different mechanisms in explaining the observed distributions are discussed.

The largest storm time increase in NO partial column at  $70\text{--}90$  km is in the  $\Lambda = -66^\circ$  to  $-70^\circ$  range, overlapping the  $\Lambda = -62^\circ$  to  $-70^\circ$  zone, where 100–300 keV electron flux is highest. The very small lag times ( $<1$  day) for NO observations within the longitude quadrant  $180^\circ$  to  $90^\circ\text{W}$  of the geomagnetic oval suggest that the substantial increases in upper mesospheric NO in this region are dominated by direct MEE electron production. For the innermost geographic latitude bin, at  $76.0^\circ\text{S}$ , observations are within the  $\Lambda = -60^\circ$  to

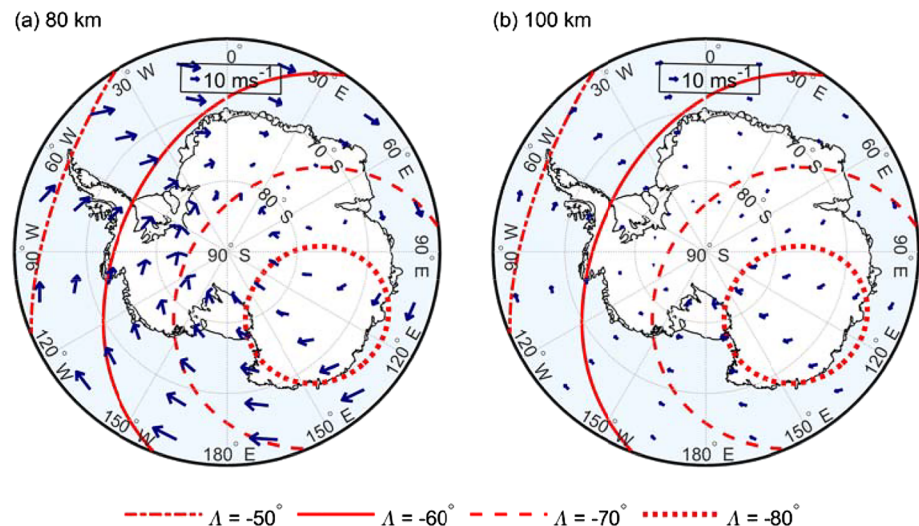


**Figure 11.** Maps of the SH and Antarctica poleward of 60°S with dark blue arrows showing horizontal wind direction and speed at altitudes of (a) 80 km and (b) 100 km, calculated using HWM14 for the main storm period (epoch days 0 to 2) of the selected geomagnetic storms. The legends in the rectangular boxes shows the arrow length corresponding to a  $10 \text{ m s}^{-1}$  wind speed. The dash-dotted, solid, dashed, and dotted red magnetic latitude lines are as described in Figure 4.

–70° oval over longitudes 150°W to 30°E. Eastward of 90°W, lag times at 76.0°S increase to 3 days, indicating that NO produced at 180° to 90°W moves rapidly eastward within the polar vortex. A similar pattern of increasing lag time is seen in the outermost geographic latitude bins, at 67.3°S, where NO is transported out of the  $\Lambda = -60^\circ$  to  $-70^\circ$  oval and reaches the Antarctic Peninsula and Weddell Sea region (60–30°W) within 2–3 days. The HWM14 calculations of uniform  $\sim 20\text{--}30 \text{ m s}^{-1}$  eastward winds at 80 km would allow horizontal transport of NO between these regions on these time scales. West Antarctica and the Peninsula are also where the strongest SH wintertime polar vortices are found. Harvey et al. (2018) showed that polar vortices tend to be oriented SE–NW in the high-latitude SH at 50 and 75 km and tilt westward with increasing altitude. Poleward of 60°S, the polar vortices at  $\sim 75 \text{ km}$  occur most frequently over the longitude segment 120–60°W. Under these circumstances, NO produced within this segment of the  $\Lambda = -60^\circ$  to  $-70^\circ$  oval, and NO transported eastward over the Antarctic Peninsula, will be more efficiently transported vertically downward to the upper stratosphere by the polar vortex, which acts as a loss mechanism for NO in the upper mesosphere.

As a result of the AIM satellite orbit, the SOFIE observations presented here do not cover the region 120°W to 0° at  $|\Lambda| > 65^\circ$ , where the geomagnetic conjugate POES data show the highest 30–300 keV precipitating electron fluxes. NO is increased where observational data are available east of this region, at 30–60°E, but not to the high levels seen at 180° to 120°W. NO production could be lower, but strong eastward winds would also introduce air from low latitudes, where MEE precipitating flux is low, into the 0–60° region and dilute the NO enhancements. Similarly, circulating high-latitude NO-poor air entering the 180° to 120°W region could explain the smaller NO increases at 71.7°S compared to the corresponding observations at lower latitudes. Another possible mechanism is associated with the auroral oval extending more equatorward during enhanced geomagnetic activity. Analysis of long-term POES data sets (van de Kamp et al., 2016) suggests that the poleward edge of the region of MEE precipitation shifts to lower  $L$  at high  $A_p$  levels. Thus, electron flux and associated NO production could be reduced at corresponding high geographic latitudes.

In the lower thermosphere, at 90–110 km, the largest storm time NO increases are at  $\Lambda = -62^\circ$  to  $-70^\circ$ , coincident in time with the highest POES 30–100 keV fluxes over these geomagnetic latitudes, and also at  $\Lambda = -52^\circ$ . The NO increases are larger than those at 70–90 km, as would be expected from the higher fluxes of energetic auroral electrons that precipitate initially at  $\Lambda = -62^\circ$  to  $-66^\circ$  and then shift to higher geomagnetic latitudes ( $\Lambda = -66^\circ$  to  $-74^\circ$ ) and persist for at least 2–4 days. The observed EEP behavior is similar to that during magnetospheric substorms that occur on much shorter time scales. During substorms, precipitation initially occurs at  $L \gtrsim 6$  and expands equatorward and poleward with time to cover the range  $L = 4.6\text{--}$



14.5 ( $|\Lambda| = 62\text{--}75^\circ$ ) (Cresswell-Moorcock et al., 2013). The initial pattern of NO distribution at 90–110 km is similar to that at 70–90 km, with the largest increases at  $150^\circ\text{W}$  to  $0^\circ$  and smaller increases at  $0^\circ$  to  $150^\circ\text{E}$ . However, the NO increases at 90–110 km occur almost immediately in all regions except at  $|\Lambda| > 80^\circ$ , where there is a  $\sim 1$  day lag after the increase in geomagnetic activity. This suggests that the observed NO increases at these altitudes are dominated by direct EEP production rather than transport, as would be expected given the weak ( $\sim 5\text{--}10\text{ m s}^{-1}$ ) eastward winds at 100 km estimated by HWM14.

Horizontal redistribution of NO in the lower thermosphere away from the main auroral source regions does not explain the substantial NO increases at  $\Lambda = -52^\circ$ . However, Kavanagh et al. (2018) showed that significant EEP  $> 30\text{ keV}$  can occur at the lower geomagnetic latitudes of the Antarctic Peninsula. According to their combined observations and model study, when the radiation belt slot region ( $L \sim 2\text{--}3$ ) fills with electrons during geomagnetic storms, increased precipitation into the mesosphere occurs over  $\sim 10$  days. These events, which are not uncommon, extend the region of potential EEP and  $\text{NO}_x$  production beyond the auroral and outer radiation belt regions. Although the mechanism would produce additional NO in the lower mesosphere, and even down to  $\sim 55\text{ km}$ , at lower altitudes (e.g., 70–90 km) the steady production over multiple days will be difficult to distinguish from NO being transported horizontally or descending in the polar vortex on similar time scales.

## 5. Conclusions

We have used a new version of the NO number density data set retrieved from SOFIE satellite observations to calculate best estimates of NO partial columns at 70–90 and 90–110 km and measurement uncertainties. Integrating the NO vertical profiles loses the original  $\sim 2\text{--}3\text{ km}$  altitude resolution of the SOFIE observations but produces partial columns with small measurement uncertainties, allowing changes in NO abundance with geographic location and geomagnetic latitude to be studied. SOFIE measurements at different locations are made at different times of day, but the data used in this study are found to be within a narrow range of MLT inside or close to the dawn sector. Thus, the observed NO distributions are not significantly affected by variations in EEP flux with MLT. Changes in the NO partial columns in the SH high-latitude ( $>60^\circ\text{S}$ ) upper mesosphere (70–90 km) and lower thermosphere (90–110 km) during EEP events have been investigated using SEA of 17 isolated wintertime (MJJA) geomagnetic storms during 2008–2014. Analysis of the SOFIE data, together with the corresponding POES observations of 30–100 and 100–300 keV electron fluxes for the SH (and NH conjugate points in SH regions affected by the SAMA), and horizontal winds from HWM14, leads to the following conclusions:

1. During geomagnetic storms, direct NO production by MEE is observed in the SH upper mesosphere (70–90 km) within the  $\Lambda = -66^\circ$  to  $-70^\circ$  zone at longitudes  $180^\circ$  to  $120^\circ\text{W}$  where SOFIE data are available. Smaller NO increases occur at  $30\text{--}60^\circ\text{E}$ , due to either lower NO production or strong eastward winds introducing air from low latitudes, where MEE precipitating flux is low, leading to dilution of the NO enhancements. Larger NO increases may occur above Antarctica at  $120^\circ\text{W}$  to  $30^\circ\text{E}$  where the flux of electrons with energies in the range 100–300 keV is likely to be highest.
2. In the lower thermosphere, at 90–110 km, the largest storm time NO increases are at  $\Lambda = -62^\circ$  to  $-70^\circ$  and also at  $\Lambda = -52^\circ$ . The NO increases are larger than those at 70–90 km, due to the higher fluxes of 30–100 keV electrons that precipitate initially at  $\Lambda = -62^\circ$  to  $-66^\circ$  and then shift to higher geomagnetic latitudes ( $\Lambda = -66^\circ$  to  $-74^\circ$ ) and persist for at least 2–4 days.
3. Strong, eastward wintertime winds in the high-latitude upper mesosphere ( $\sim 20\text{--}30\text{ m s}^{-1}$  at 80 km) provide an efficient mechanism for transporting NO-enriched air away from source regions over 1–3 days. The circumpolar winds in the middle atmosphere may also introduce NO-poor air from outside the source regions, offsetting NO increases. The lower thermospheric eastward winds are lighter ( $\sim 5\text{--}10\text{ m s}^{-1}$  at 100 km), and NO increases above  $\sim 90\text{ km}$  are likely to be dominated by direct EEP production rather than horizontal transport.

Our analysis employs SOFIE observations made during SH winters, when NO is long-lived in darkness at high latitudes. This accumulation of NO leads to readily observable increases in the wintertime middle atmosphere, which is advantageous for characterizing EEP effects arising from weak to moderate geomagnetic storm activity. However, the long lifetime of NO, the presence of strong horizontal winds, and downward transport in the polar vortex during winter also complicate the assignment of direct NO

production versus transported NO. The analysis methods used in this work could be applied in further studies of NO distributions, for example, during months outside of winter when NO increases are short-lived. Such future studies would benefit from already available long time series data sets from SOFIE and any other additional satellite and ground-based instruments that provide observations with adequate sensitivity and coverage, as well as model developments to test and verify the different EEP production and transport mechanisms.

## Data Availability Statement

The AIM-SOFIE data are found online at <http://sofie.gats-inc.com>. Processed data sets (Newnham et al., 2020) from this study are available via the UK Polar Data Centre's Discovery Metadata System (<https://data.bas.ac.uk/>).

## Acknowledgments

This work was supported in part by the UK Research and Innovation Natural Environment Research Council (Grant References NE/J022187/1 and NE/R016038/1) and the New Zealand Marsden Fund. D. R. M. was supported in part by NASA Living With a Star Grant NNX14AH54G. The National Center for Atmospheric Research (NCAR) is sponsored by the U.S. National Science Foundation (NSF). Aaron Hendry is thanked for providing computer code (GEO2CGM) for converting spherical geographic coordinates to spherical corrected geomagnetic coordinates. NOAA's National Geophysical Data Center is acknowledged for providing the NOAA POES data (available from <https://www.ngdc.noaa.gov/stp/satellite/poes/index.html>).

## References

- Allison, H. J., Horne, R. B., Glauert, S. A., & Del Zanna, G. (2017). The magnetic local time distribution of energetic electrons in the radiation belt region. *Journal of Geophysical Research: Space Physics*, 122, 8108–8123. <https://doi.org/10.1002/2017JA024084>
- Andersson, M. E., Verronen, P. T., Marsh, D. R., Seppälä, A., Pääväranta, S.-M., Rodger, C. J., & van de Kamp, M. (2018). Polar ozone response to energetic particle precipitation over decadal time scales: The role of medium-energy electrons. *Journal of Geophysical Research: Atmospheres*, 123, 607–622. <https://doi.org/10.1002/2017JD027605>
- Andersson, M. E., Verronen, P. T., Rodger, C. J., Clilverd, M. A., & Wang, S. (2014). Longitudinal hotspots in the mesospheric OH variations due to energetic electron precipitation. *Atmospheric Chemistry and Physics*, 14(2), 1095–1105. <https://doi.org/10.5194/acp-14-1095-2014>
- Arsenovic, P., Damiani, A., Rozanov, E., Funke, B., Stenke, A., & Peter, T. (2019). Reactive nitrogen (NO<sub>x</sub>) and ozone responses to energetic electron precipitation during Southern Hemisphere winter. *Atmospheric Chemistry and Physics*, 19(14), 9485–9494. <https://doi.org/10.5194/acp-19-9485-2019>
- Arsenovic, P., Rozanov, E., Stenke, A., Funke, B., Wissing, J. M., Mursula, K., et al. (2016). The influence of middle range energy electrons on atmospheric chemistry and regional climate. *Journal of Atmospheric and Solar-Terrestrial Physics*, 149, 180–190. <https://doi.org/10.1016/j.jastp.2016.04.008>
- Baker, D. N., Erickson, P. J., Fennell, J. F., Foster, C., Jaynes, A. N., & Verronen, P. T. (2018). Space weather effects in the Earth's radiation belts. *Space Science Reviews*, 214(1), 17. <https://doi.org/10.1007/s11214-017-0452-7>
- Barth, C. A., & Bailey, S. M. (2004). Comparison of a thermospheric photochemical model with student nitric oxide explorer (SNOE) observations of nitric oxide. *Journal of Geophysical Research*, 109, A03304. <https://doi.org/10.1029/2003JA010227>
- Barth, C. A., Mankoff, K. D., Bailey, S. M., & Solomon, S. C. (2003). Global observations of nitric oxide in the thermosphere. *Journal of Geophysical Research*, 108(A1), 1027. <https://doi.org/10.1029/2002JA009458>
- Baumgaertner, A. J. G., Seppälä, A., Jöckel, P., & Clilverd, M. A. (2011). Geomagnetic activity related NO<sub>x</sub> enhancements and polar surface air temperature variability in a chemistry climate model: Modulation of the NAM index. *Atmospheric Chemistry and Physics*, 11(9), 4521–4531. <https://doi.org/10.5194/acp-11-4521-2011>
- Bender, S., Sinnhuber, M., Espy, P. J., & Burrows, J. P. (2019). Mesospheric nitric oxide model from SCIAMACHY data. *Atmospheric Chemistry and Physics*, 19(4), 2135–2147. <https://doi.org/10.5194/acp-19-2135-2019>
- Brasseur, G. P., & Solomon, S. (2005). *Aeronomy of the middle atmosphere* (3rd ed.). Dordrecht, The Netherlands: Springer. <https://doi.org/10.1007/1-4020-3824-0>
- Cresswell-Moorcock, K., Rodger, C. J., Kero, A., Collier, A. B., Clilverd, M. A., Häggström, I., & Pitkänen, T. (2013). A reexamination of latitudinal limits of substorm produced energetic electron precipitation. *Journal of Geophysical Research: Space Physics*, 118, 6694–6705. <https://doi.org/10.1002/jgra.50598>
- Davis, T. N., & Sugiura, M. (1966). Auroral electrojet activity index AE and its universal time variations. *Journal of Geophysical Research*, 71(3), 785–801. <https://doi.org/10.1029/JZ071i003p00785>
- Dieminger, W., Hartmann, G. K., & Leitinger, R. (1996). Geomagnetic activity indices. In W. Dieminger, G. Hartmann, & R. Leitinger (Eds.), *The upper atmosphere*, edited by, (pp. 887–911). Berlin: Springer. <https://doi.org/10.1007/978-3-642-78717-1>
- Drob, D. P., Emmert, J. T., Meriwether, J. W., Makela, J. J., Doornbos, E., Conde, M., et al. (2015). An update to the Horizontal Wind Model (HWM): The quiet time thermosphere. *Earth and Space Science*, 2, 301–319. <https://doi.org/10.1002/2014EA000089>
- Evans, D. S., & Greer, M. S. (2004). *Polar Orbiting Environmental Satellite Space Environment Monitor—2 Instrument descriptions and archive data documentation*. NOAA Technical Memorandum Version 1.4. Boulder, CO: Space Environment Laboratory.
- Funke, B., Ball, W., Bender, S., Gardini, A., Harvey, V. L., Lambert, A., et al. (2017). HEPPA-II model-measurement intercomparison project: EPP indirect effects during the dynamically perturbed NH winter 2008–2009. *Atmospheric Chemistry and Physics*, 17(5), 3573–3604. <https://doi.org/10.5194/acp-17-3573-2017>
- Gordley, L. L., Hervig, M. E., Fish, C., Russell, J. M. III, Cook, J., Hanson, S., et al. (2009). The Solar Occultation For Ice Experiment (SOFIE). *Journal of Atmospheric and Solar-Terrestrial Physics*, 71(3–4), 300–315. <https://doi.org/10.1016/j.jastp.2008.07.012>
- Harvey, V. L., Randall, C. E., Goncharenko, L., Becker, E., & France, J. (2018). On the upward extension of the polar vortices into the mesosphere. *Journal of Geophysical Research: Atmospheres*, 123, 9171–9191. <https://doi.org/10.1029/2018JD028815>
- Hendrickx, K., Megner, L., Gumbel, J., Siskind, D. E., Orsolini, Y. J., Nesse Tysøy, H., & Hervig, M. (2015). Observations of 27 day solar cycles in the production and mesospheric descent of EPP-produced NO. *Journal of Geophysical Research: Space Physics*, 120, 8978–8988. <https://doi.org/10.1002/2015JA021441>
- Hendrickx, K., Megner, L., Marsh, D. R., Gumbel, J., Strandberg, R., & Martinsson, F. (2017). Relative importance of nitric oxide physical drivers in the lower thermosphere. *Geophysical Research Letters*, 44, 10,081–10,087. <https://doi.org/10.1002/2017GL074786>
- Hendrickx, K., Megner, L., Marsh, D. R., & Smith-Johnsen, C. (2018). Production and transport mechanisms of NO in the polar upper mesosphere and lower thermosphere in observations and models. *Atmospheric Chemistry and Physics*, 18(12), 9075–9089. <https://doi.org/10.5194/acp-18-9075-2018>

- Hendry, A. T., Rodger, C. J., & Clilverd, M. A. (2017). Evidence of sub-MeV EMIC-driven electron precipitation. *Geophysical Research Letters*, 44, 1210–1218. <https://doi.org/10.1002/2016GL071807>
- Hervig, M. E., Marshall, B. T., Bailey, S. M., Siskind, D. E., Russell, J. M. III, Bardeen, C. G., et al. (2019). Validation of Solar Occultation for Ice Experiment (SOFIE) nitric oxide measurements. *Atmospheric Measurement Techniques*, 12(6), 3111–3121. <https://doi.org/10.5194/amt-12-3111-2019>
- Horne, R. B., Lam, M. M., & Green, J. C. (2009). Energetic electron precipitation from the outer radiation belt during geomagnetic storms. *Geophysical Research Letters*, 36, L19104. <https://doi.org/10.1029/2009GL040236>
- Horne, R. B., Thorne, R. M., Shprits, Y. Y., Meredith, N. P., Glauert, S. A., Smith, A. J., et al. (2005). Wave acceleration of electrons in the Van Allen radiation belts. *Nature*, 437(7056), 227–230. <https://doi.org/10.1038/nature03939>
- Ipavich, F. M., Galvin, A. B., Lasley, S. E., Paquette, J. A., Hefti, S., Reiche, K.-U., et al. (1998). Solar wind measurements with SOHO: The CELIAS/MTOF proton monitor. *Journal of Geophysical Research*, 103(A8), 17,205–17,213. <https://doi.org/10.1029/97JA02770>
- Isono, Y., Mizuno, A., Nagahama, T., Miyoshi, Y., Nakamura, T., Kataoka, R., et al. (2014). Variations of nitric oxide in the mesosphere and lower thermosphere over Antarctica associated with a magnetic storm in April 2012. *Geophysical Research Letters*, 41, 2568–2574. <https://doi.org/10.1002/2014GL059360>
- Jackman, C. H., & McPeters, R. D. (2004). The effect of solar proton events on ozone and other constituents. In *Solar variability and its effects on climate*, *Geophysical Monograph Series* (Vol. 141, pp. 305–319). Washington, DC: American Geophysical Union. <https://doi.org/10.1029/141GM21>
- Kavanagh, A. J., Cobbett, N., & Kirsch, P. (2018). Radiation belt slot region filling events: Sustained energetic precipitation into the mesosphere. *Journal of Geophysical Research: Space Physics*, 123, 7999–8020. <https://doi.org/10.1029/2018JA025890>
- Kivelson, M., & Russell, C. (1995). *Introduction to space physics* (pp. 166–167). New York, NY: Cambridge University Press.
- Kiviranta, J., Pérot, K., Eriksson, P., & Murtagh, D. (2018). An empirical model of nitric oxide in the upper mesosphere and lower thermosphere based on 12 years of Odin SMR measurements. *Atmospheric Chemistry and Physics*, 18(18), 13393–13410. <https://doi.org/10.5194/acp-18-13393-2018>
- Kovács, T., Plane, J. M. C., Feng, W., Nagy, T., Chipperfield, M. P., Verronen, P. T., et al. (2016). D-region ion–neutral coupled chemistry (Sodankylä Ion Chemistry, SIC) within the Whole Atmosphere Community Climate Model (WACCM 4)—WACCM-SIC and WACCM-rSIC. *Geoscientific Model Development*, 9(9), 3123–3136. <https://doi.org/10.5194/gmd-9-3123-2016>
- Lee, J.-H., Jee, G., Kwak, Y. S., Hong, S. B., Hwang, H., Song, I. S., et al. (2018). Responses of Nitrogen Oxide to High-Speed Solar Wind Stream in the Polar Middle Atmosphere. *Journal of Geophysical Research: Space Physics*, 123, 9788–9801. <https://doi.org/10.1029/2017JA025161>
- Marsh, D. R., Mills, M. J., Kinnison, D. E., & Lamarque, J.-F. (2013). Climate change from 1850 to 2005 simulated in CESM1 (WACCM). *Journal of Climate*, 26(19), 7372–7391. <https://doi.org/10.1175/JCLI-D-12-00558.1>
- Marsh, D. R., Solomon, S. C., & Reynolds, A. E. (2004). Empirical model of nitric oxide in the lower thermosphere. *Journal of Geophysical Research*, 109, A07301. <https://doi.org/10.1029/2003JA010199>
- Matthes, K., Funke, B., Andersson, M. E., Barnard, L., Beer, J., Charbonneau, P., et al. (2017). Solar forcing for CMIP6 (v3.2). *Geoscientific Model Development*, 10(6), 2247–2302. <https://doi.org/10.5194/gmd-10-2247-2017>
- McIlwain, C. E. (1961). Coordinates for mapping the distribution of magnetically trapped particles. *Journal of Geophysical Research*, 66(11), 3681–3691. <https://doi.org/10.1029/JZ066i011p03681>
- Mironova, I. A., Aplin, K. L., Arnold, F., Bazilevskaya, G. A., Harrison, R. G., Krivolutsky, A. A., et al. (2015). Energetic particle influence on the Earth's atmosphere. *Space Science Reviews*, 194(1–4), 1–96. <https://doi.org/10.1007/s11214-015-0185-4>
- Newnham, D. A., Clilverd, M. A., Rodger, C. J., Hendrickx, K., Megner, L., Kavanagh, A. J., et al. (2018). Observations and modeling of increased nitric oxide in the Antarctic polar middle atmosphere associated with geomagnetic storm-driven energetic electron precipitation. *Journal of Geophysical Research: Space Physics*, 123, 6009–6025. <https://doi.org/10.1029/2018JA025507>
- Newnham, D. A., Rodger, C. J., & Hervig, M. E. (2020). *Atmospheric observational and model datasets: Spatial distributions of nitric oxide (NO) in the winter time, high latitude southern hemisphere atmosphere [data set]*. UK Polar Data Centre, Natural Environment Research Council, UK Research & Innovation. <https://doi.org/10.5285/0DF08DF3-8453-4CC0-A79D-70FED11ED220>
- Palmer, P. I. (2014). *Essential maths for geoscientists: An introduction*. New York, NY: Wiley-Blackwell.
- Pettit, J. M., Randall, C. E., Peck, E. D., Marsh, D. R., Kamp, M., Fang, X., et al. (2019). Atmospheric effects of >30 keV energetic electron precipitation in the Southern Hemisphere winter during 2003. *Journal of Geophysical Research: Space Physics*, 124, 8138–8153. <https://doi.org/10.1029/2019JA026868>
- Rodger, C. J., Clilverd, M. A., Green, J. C., & Lam, M. M. (2010). Use of POES SEM-2 observations to examine radiation belt dynamics and energetic electron precipitation into the atmosphere. *Journal of Geophysical Research*, 115, A04202. <https://doi.org/10.1029/2008JA014023>
- Rodger, C. J., Kavanagh, A. J., Clilverd, M. A., & Marple, S. R. (2013). Comparison between POES energetic electron precipitation observations and riometer absorptions: Implications for determining true precipitation fluxes. *Journal of Geophysical Research: Space Physics*, 118, 7810–7821. <https://doi.org/10.1002/2013JA019439>
- Semeniuk, K., Fomichev, V. I., McConnell, J. C., Fu, C., Melo, S. M. L., & Usoskin, I. G. (2011). Middle atmosphere response to the solar cycle in irradiance and ionizing particle precipitation. *Atmospheric Chemistry and Physics*, 11(10), 5045–5077. <https://doi.org/10.5194/acp-11-5045-2011>
- Seppälä, A., Clilverd, M. A., Beharrell, M. J., Rodger, C. J., Verronen, P. T., Andersson, M. E., & Newnham, D. A. (2015). Substorm-induced energetic electron precipitation: Impact on atmospheric chemistry. *Geophysical Research Letters*, 42, 8172–8176. <https://doi.org/10.1002/2015GL065523>
- Seppälä, A., Lu, H., Clilverd, M. A., & Rodger, C. J. (2013). Geomagnetic activity signatures in wintertime stratosphere wind, temperature, and wave response. *Journal of Geophysical Research: Atmospheres*, 118, 2169–2183. <https://doi.org/10.1002/jgrd.50236>
- Seppälä, A., Randall, C. E., Clilverd, M. A., Rozanov, E., & Rodger, C. J. (2009). Geomagnetic activity and polar surface air temperature variability. *Journal of Geophysical Research*, 114, A10312. <https://doi.org/10.1029/2008JA014029>
- Shimazaki, T. (1984). The photochemical time constants of minor constituents and their families in the middle atmosphere. *Journal of Atmospheric and Terrestrial Physics*, 46(2), 173–191. [https://doi.org/10.1016/0021-9169\(84\)90143-0](https://doi.org/10.1016/0021-9169(84)90143-0)
- Sinnhuber, M., Nieder, H., & Wieters, N. (2012). Energetic particle precipitation and the chemistry of the mesosphere/lower thermosphere. *Surveys in Geophysics*, 33(6), 1281–1334. <https://doi.org/10.1007/s10712-012-9201-3>
- Smith-Johnsen, C., Marsh, D. R., Orsolini, Y., Nesse Tysøy, H., Hendrickx, K., Sandanger, M. I., et al. (2018). Nitric oxide response to the April 2010 electron precipitation event—Using WACCM and WACCM-D with and without medium energy electrons. *Journal of Geophysical Research: Space Physics*, 123, 5232–5245. <https://doi.org/10.1029/2018JA025418>



- Smith-Johnsen, C., Nesse Tysøy, H., Hendrickx, K., Orsolini, Y., Kishore Kumar, G., Ødegaard, L.-K. G., et al. (2017). Direct and indirect electron precipitation effect on nitric oxide in the polar middle atmosphere, using a full-range energy spectrum. *Journal of Geophysical Research: Space Physics*, 122, 8679–8693. <https://doi.org/10.1002/2017JA024364>
- Solomon, S., Crutzen, P. J., & Roble, R. G. (1982). Photochemical coupling between the thermosphere and the lower atmosphere: 1. Odd nitrogen from 50 to 120 km. *Journal of Geophysical Research*, 87(C9), 7206–7220. <https://doi.org/10.1029/JC087iC09p07206>
- Thébault, E., Finlay, C. C., Beggan, C. D., Alken, P., Aubert, J., Barrois, O., et al. (2015). International Geomagnetic Reference Field: The 12th generation. *Earth, Planets and Space*, 67(1), 1, 79–19. <https://doi.org/10.1186/s40623-015-0228-9>
- Turunen, E., Verronen, P. T., Seppälä, A., Rodger, C. J., Clilverd, M. A., Tamminen, J., et al. (2009). Impact of different precipitation energies on NO<sub>x</sub> generation during geomagnetic storms. *Journal of Atmospheric and Solar-Terrestrial Physics*, 71(10-11), 1176–1189. <https://doi.org/10.1016/j.jastp.2008.07.005>
- van de Kamp, M., Rodger, C. J., Seppälä, A., Clilverd, M. A., & Verronen, P. T. (2018). An updated model providing long-term data sets of energetic electron precipitation, including zonal dependence. *Journal of Geophysical Research: Atmospheres*, 123, 9891–9915. <https://doi.org/10.1029/2017JD028253>
- van de Kamp, M., Seppälä, A., Clilverd, M. A., Rodger, C. J., Verronen, P. T., & Whittaker, I. (2016). A model providing long-term datasets of energetic electron precipitation during geomagnetic storms. *Journal of Geophysical Research: Atmospheres*, 121, 12,520–12,540. <https://doi.org/10.1002/2015JD024212>
- Verronen, P. T., Andersson, M. E., Marsh, D. R., Kovács, T., & Plane, J. M. C. (2016). WACCM-D—Whole Atmosphere Community Climate Model with D-region ion chemistry. *Journal of Advances in Modeling Earth Systems*, 8, 954–975. <https://doi.org/10.1002/2015MS000592>
- Whittaker, I. C., Rodger, C. J., Clilverd, M. A., & Sauvaud, J. -A. (2014). The effects and correction of the geometric factor for the POES/MEPED electron flux instrument using a multisatellite comparison. *Journal of Geophysical Research: Space Physics*, 119, 6386–6404. <https://doi.org/10.1002/2014JA020021>
- Yokoyama, N., & Kamide, Y. (1997). Statistical nature of geomagnetic storms. *Journal of Geophysical Research*, 102(A7), 14,215–14,222. <https://doi.org/10.1029/97JA00903>
- Zawedde, A. E., Nesse Tysøy, H., Stadsnes, J., & Sandanger, M. I. (2019). Are EEP events important for the tertiary ozone maximum? *Journal of Geophysical Research: Space Physics*, 124, 5976–5994. <https://doi.org/10.1029/2018JA02620>